



Low-temperature processed highly efficient hole transport layer free carbon-based planar perovskite solar cells with SnO₂ quantum dot electron transport layer

S.N. Vijayaraghavan ^{a,1}, J. Wall ^{a,1}, L. Li ^a, G. Xing ^b, Q. Zhang ^c, F. Yan ^{a, d,*}

^a Department of Metallurgical and Materials Engineering, The University of Alabama, Tuscaloosa, AL, 35487, USA

^b Key Laboratory of Microelectronic Devices & Integrated Technology, Institute of Microelectronics, Chinese Academy of Sciences, Beijing, 100029, China

^c Department of Materials Science and Engineering, Harbin University of Technology, Shenzhen, 518055, China

^d Alabama Water Institute, The University of Alabama, Tuscaloosa, AL, 35487, USA



ARTICLE INFO

Article history:

Received 2 February 2020

Received in revised form

23 February 2020

Accepted 25 February 2020

Available online 5 March 2020

Keywords:

SnO₂ quantum dot

Planar perovskite solar cells

Carbon electrode

Hole transport layer free

Low-temperature process

ABSTRACT

The use of expensive hole transport layers (HTLs) and back contact along with the stability issue of perovskite solar cells (PSCs) has been a detrimental factor when it comes to commercialization of the technology. In addition, high temperature and long annealing time processed electron transport layers (ETLs, e.g. TiO₂) prevent the flexible solar cell application in most polymer substrates. Herein, we opted for HTL-free carbon electrodes owing to their low-cost production and superior stability in air, compared with their noble metal counterparts. In this work, we fabricate planar PSCs using low-temperature solution processed SnO₂ quantum dots (QDs) as ETLs, which offers significant advantages over high-temperature processed ETLs because of its excellent electron extraction and hole blocking ability. In addition, by integrating a low-cost and stable carbon electrode, an impressive energy conversion efficiency of 13.64% with a device architecture glass/In doped SnO₂/QD-SnO₂/perovskite/carbon under 1 sun illumination at ambient conditions have been achieved. This work paves the way to achieve fully low-temperature processed printable PSCs at an affordable cost by integrating the QD SnO₂ ETL and carbon electrodes.

© 2020 Elsevier Ltd. All rights reserved.

1. Introduction

Photovoltaic devices such as solar cells are used to efficiently convert solar energy into useful electrical energy. More than 90% of the installed solar modules use crystalline silicon panels [1]. In the last few decades, new technologies such as organic photovoltaics, excitonic solar cells, and thin-film modules have been developed to keep costs low and to boost the device performance beyond conventional efficiency limits [2–9]. Perovskite solar cells (PSCs), with an inorganic-organic hybrid absorber (e.g. CH₃NH₃PbI₃), have demonstrated a power conversion efficiency (PCE) from ~3.8% to an impressive 25.2% in less than one decade [10–13]. The rapid development of PSCs has turned heads in the solar industry as it has the potential for replacing the conventional photovoltaic devices,

such as Si and CdTe. Going by the theoretical prediction, a single-junction PSC can attain PCEs as high as 33.5%, surpassing the well-established copper indium gallium selenide and CdTe-based solar cells [14]. The hybrid PSCs have gathered attention not only because of their sky-rocketing PCEs but also because of the low-cost materials and synthesis techniques involved as it makes use of simple solution-processing techniques, such as roll-to-roll processing [15,16].

For the highly efficient planar solar cell architecture, either the regular or inverted structure, the PSC layer was switched between an ETL and a HTL. The ETL is an indispensable component to select electrons and block holes while the HTL is desired to collect the holes and form a barrier for the electron transport. Thus, improving the performance of PSCs starts with proper choice of ETLs and HTLs and optimizing their processing conditions. To date, most PSCs use compact layers and mesoporous scaffolds of TiO₂ as an ETL, and it has resulted in an impressive PCE (up to 25.2%) through various material and structural optimizations [15–20]. Despite numerous advantages that TiO₂ possesses, one major disadvantage to scale up

* Corresponding author.

E-mail address: fyan4@ua.edu (F. Yan).

¹ Contributions: S. N. Vijayaraghavan and J. Wall contributed equally to this work.

the TiO_2 -based PSC is its high processing temperature ($>450^\circ\text{C}$) and long durations for sintering to fully crystallize into the desired polymorph, which translates into high costs and high energy consumption while also hampering the possibility of developing flexible PSCs on most of the low-melting-point polymer substrates [21]. TiO_2 also suffers from poor optoelectronic properties including poor conductivity and mobility [22–24]. Moreover, using TiO_2 compromises long-term stability as it is prone to photocatalysis under UV illumination [22,25,26]. To address these concerns, replacing TiO_2 with SnO_2 in planar PSCs plays as an effective way to reduce the annealing time and temperature and to improve the stability and efficiency [27–29]. In particular, photophysical benefit from SnO_2 ETL includes excellent charge mobility, wider bandgap, low-temperature synthesis, and a favorable band energy alignment [30,31]. The excellent electron mobility and wider bandgap contributes to more efficient charge transport from the absorber layer to SnO_2 , which contributes toward improved PCEs. However, SnO_2 comes with its own set of issues. For instance, solution-processed SnO_2 cannot be fully crystallized at low annealing temperatures ($<200^\circ\text{C}$) which in turn takes a toll on the electron mobility. If the annealing temperature is increased to fully crystallize the film, it may result in film breakdown [32]. The annealing temperature can be reduced by using the low-temperature processed colloidal nanoparticles, thereby overcoming this dilemma. While the colloidal SnO_2 solution may suffer from long-term stability issues, SnO_2 quantum dots (QDs) have been extensively explored in PSCs, due to their higher molar extinction coefficients, tunable photo-response, strong light scattering ability, fast electron transport, and slow recombination, resulting in a dramatic increase in PCE [33–37].

Most commonly used HTLs are organics, such as spiro-OMeTAD and P3HT, and are usually unstable and much more expensive than perovskite materials. Hence, it is desired to eliminate HTLs from PSC architecture to reduce the complexity and the cost of the device fabrication process. By reducing one step of the standard coating process, at least one-third of the manufacturing cost and time can be saved, in addition to savings of material cost for HTLs [38–42]. The noble metal electrode, for example, Au and Ag, also adds to the cost of the device as the metal itself is expensive and it requires to be thermally evaporated in vacuum. These mounting costs will hinder the progress of PSCs toward affordable commercialization. Hence, it becomes imperative to address these challenges by combinations of HTLs with back contact that can also be efficiently used for large-scale deployment of PSCs [43–45]. Fortunately, perovskites are so unique that it can also serve as an HTL because of its ambipolar nature, thereby enabling HTL-free PSCs [46–50]. And these aforementioned issues prompted the researchers to explore the promise offered by carbon-based perovskites as it is earth abundant, low cost, environmentally stable, and conductive [20,51–54]. In particular, the conventional precious HTL-free device is desired to reduce the cost of the PSCs.

Carbon electrode is considered to be the most promising electrode for the back contact as it is cheap, stable, inert to ion migration from perovskite, and inherently water resistant which acts as a protection for the perovskite layer from the moisture [55,56]. But carbon comes along with a set of disadvantages such as low conductivity and the need for HTLs for highly efficient carbon-based PSCs. Although the stability of the carbon-based PSCs is far superior than that of the traditional PSCs, the long-term stability still lags when compared with that of the well-established inorganic solar cells, such as Si, and CdTe solar cells. Ku et al. [52] were the first to use spheroidal graphite and carbon black as a substitute for HTLs and the metal cathode. The fabricated cell reported a PCE of 6.6%, and it was a breakthrough in

PSCs that resulted in the evolution of HTL and metal electrode-free PSCs. Since then several forms of carbon such as single-walled and multi-walled carbon nanotubes, graphite powder, carbon cloth carbon black, and so on have been used in HTL and metal electrode-free PSCs [57–61]. Within a short span of time, the PCE of carbon-based PSCs have drastically increased from 6.6% to 17%. But most of the reported work requires the HTL along with carbon [62,63].

Based on the well-established fabrication techniques for high-efficiency PSCs, the fabrication process can be made scalable for flexible devices via roll-to-roll processing by opting for materials that require low processing temperatures ($<200^\circ\text{C}$) and printing or coating of the back electrode with good contact to the absorber layer without damaging it. Through our work, we address the usage of low-temperature processed materials by replacing the commonly used mesoporous TiO_2 as the ETL with SnO_2 QDs. And we substitute the commonly used vacuum-deposited back electrode with low-temperature curable carbon electrode. In this work, we develop a fully low-temperature processed carbon-based HTL-free planar PSC with a PCE of $\sim 13.64\%$ by integrating SnO_2 QD ETLs. The processing temperature for the whole device, glass/ITO/ SnO_2 /perovskite/carbon, never exceeded 180°C . This study demonstrates printability for the flexible carbon-based low-cost PSCs on the polymer substrate.

2. Experimental section

2.1. Materials

PbI_2 (Sigma-Aldrich, 99.999%), PbBr_2 (Alfa Aesar, 99.98%), formamidinium iodide (FAI, GreatCellSolar), methylammonium bromide (MABr, GreatCellSolar), CsI (BeanTown Chemical, 99.9%), $\text{SnCl}_2 \cdot 2\text{H}_2\text{O}$ (Acros Organics, 97%), and thiourea (Alfa Aesar, 99%) were used as received. Dimethyl sulfoxide (DMSO) and dimethyl formamide (DMF) were purchased from Sigma-Aldrich and used without further purification.

2.2. Perovskite precursor preparation

The $\text{Cs}_{0.05}\text{FA}_{0.81}\text{MA}_{0.14}\text{PbI}_{2.55}\text{Br}_{0.45}$ precursor solution was prepared with corresponding molar ratios of PbI_2 (1.1 M), PbBr_2 (0.2 M), FAI (1 M), MABr (0.2 M), and CsI (1.5 M in DMSO) dissolved in a mixed solvent of DMF and DMSO with a volume ratio of 4:1. The prepared perovskite precursor was then stirred at 70°C .

2.3. Solar cell fabrication

ITO substrates were successively cleaned by sonication with detergent solution, deionized water (DIW), acetone, and isopropanol followed by a UV-ozone treatment for 30 min. The SnO_2 QDs were synthesized at room temperature following the previous report [36]. A 0.15 M solution of $\text{SnCl}_2 \cdot 2\text{H}_2\text{O}$ in DIW with the presence of thiourea ($\text{CH}_4\text{N}_2\text{S}$) as reaction accelerator and stabilizer was prepared. The aggregation of SnO_2 QDs is inhibited by the amino groups surrounding the QDs which limits the size of the QDs to 3–5 nm. This solution is filtered with 0.45 μm PTFE filter before use. The SnO_2 layer was then spin coated using the SnO_2 QD solution. The as-deposited ETL was annealed at 180°C for 1 h in ambient. The ITO substrate was then transferred into a nitrogen-filled glovebox for coating the perovskite layer. The triple cation perovskite film was then deposited onto the ETL-coated ITOs by a two-step spin-coating procedure. The first step was 1000 r.p.m. 10 s followed by 6000 r.p.m. 20 s. Diethyl ether was dropped on the spinning ITOs during the high-speed rotation 5 s before the end of the spin coating. The deposited films were then

transferred to a hot plate and annealed at 100 °C for 30 min. Finally, after cooling down to room temperature, carbon paste was doctor bladed on top of the perovskite layer and the cells were then annealed at 100 °C for 10 min to cure the carbon electrode.

2.4. Materials and device characterization

The surface morphology of the perovskite film and carbon electrode along with the cross-sectional view of the device was characterized by the Thermo Scientific Apreo scanning electron microscopy (SEM). The electron beam was accelerated at 10 kV and 5 kV for the surface morphology and cross-sectional view, respectively. Surface roughness and particle size were analyzed using Park XE-70 atomic force microscope. A Philips X'Pert Materials Research Diffractometer using 45 kV, 40 mA Cu K α radiation ($\lambda = 0.15405$ nm) was used to measure the crystal structures of SnO₂ QDs and perovskite films. Four-point probe station was used to measure the sheet resistivity of the films. The Raman spectra of the perovskite film were measured with excitation at a wavelength of 532 nm in room temperature and ambient conditions using a LabRAM HR 800 Raman spectrometer. The X-ray photoelectron spectroscopy (XPS) was performed in a Krato Axis XPS system equipped with a monochromated Al X-ray source. The electrical characteristics were obtained using a solar simulator (Newport, Oriel Class AAA 94063A, 1000-Watt Xenon light source) with a Keithley 2420 source meter under simulated AM 1.5G (100 mW/cm²) solar irradiation. The light intensity was calibrated using a silicon reference cell (Newport, 91150V, certified by National Renewable Energy Lab). The current-voltage scan rate was

100 mVs⁻¹. The masked active area is 0.08 cm². The external quantum efficiency (EQE) was obtained by an EnliTech QE measurement system.

3. Results and discussion

X-ray diffraction (XRD) pattern of the photoanode (ITO, SnO₂, and perovskite layers) is shown in Fig. 1a. The (200) peak at 2θ ~ 37.4° indicates that the SnO₂ QDs ETL is highly crystalline with a tetragonal rutile structure. The perovskite film presents cubic crystalline structure and is in agreement with the reported triple perovskite structure. The presence of the XRD peaks of photo-inactive cubic PbI₂ ~ 12.38° suggests that extra PbI₂ exist in the perovskite films, which is due to the excess Pb that was introduced in the precursor. The excess PbI₂ could suppress the degradation of the perovskite film and increase the reliability when exposed in ambient. It is reported that moderate residues of PbI₂ in the absorber layer can effectively passivate grain boundaries, thereby reducing the defects in the material and hence improve the device performance [64–66]. In addition, the FAPbI₃ peak (2θ ~ 11.28°) may indicate the decomposition of the perovskite film upon exposure to the ambient conditions while the sample was being transferred from the N₂-filled glovebox to the XRD instrument or decompose during the XRD measurement with humidity ~50% RH.

To investigate the morphology of QD SnO₂-coated ITO substrate, atomic force microscopy (AFM) was used to record the nanometric dimensional surface roughness and to visualize the surface nanotexture of the deposited QD SnO₂ ETL films, as shown in Fig. 1b. The sphere-like structures represent the SnO₂ QDs at the substrate surface. The AFM image shows well-dispersed SnO₂ QDs. A

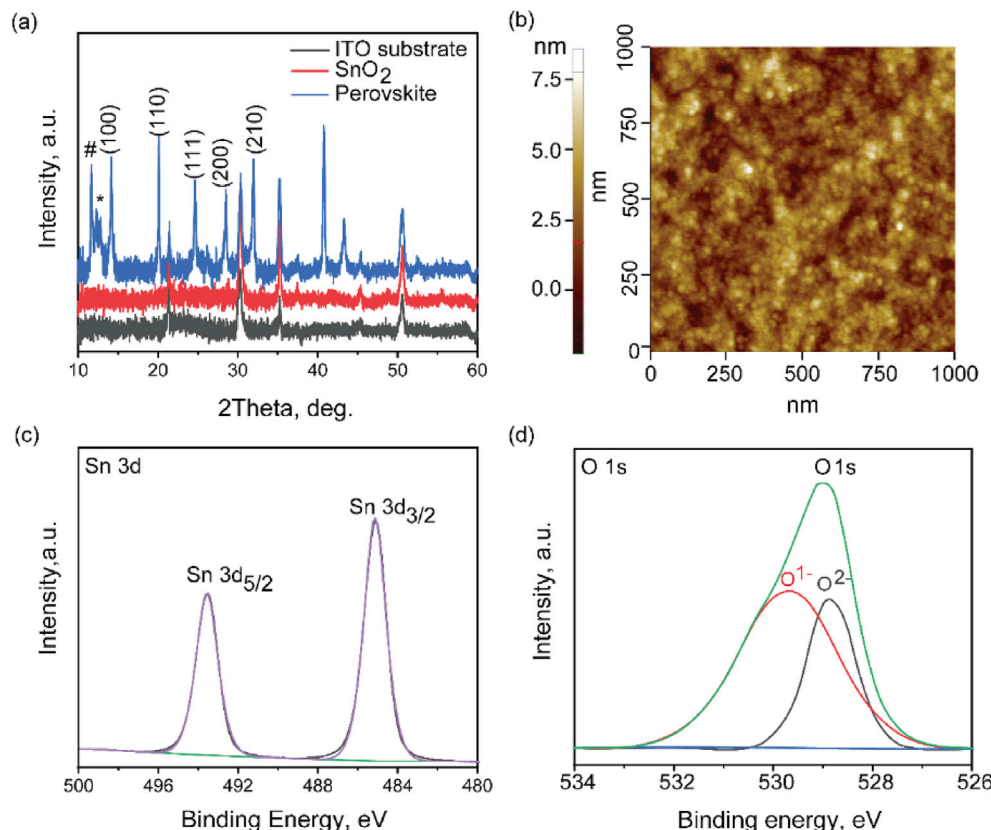


Fig. 1. (a) X-ray diffractogram of the different layers in the photoanode, where the perovskite shows the photoinactive δ-FAPbI₃ and the cubic PbI₂ marked by # and *, respectively; (b) AFM topography map of the SnO₂ QD coated ITO; (c) and (d) shows high-resolution XPS scan to examine the Sn 3d and O 1s states, respectively. AFM, atomic force microscopy; QD, quantum dot; XPS, X-ray photoelectron spectroscopy.

relatively small QD-sized distribution with an average size of 3 nm was observed. The SnO₂ QDs were found to be clustered together and well connected with each other which play a key role in transfer of the charge carriers from one QD to the adjacent one. The films were also found to be dense with no pinholes in between. The root mean square (RMS) surface roughness of the QD SnO₂ film was found to be 1.67 nm which demonstrates that our SnO₂ QD synthesis and deposition technique gave us a uniform, high quality, and smooth ETL. The surface roughness of the SnO₂ coated ITO surface is reduced compared to the ITO substrate (RMS ~ 2.99 nm, see the Fig. S1 in supporting information). A smoother surface of QD SnO₂ layer plays a vital role in determining the device performance, especially its electrical properties. A smoother surface inhibits the formation of electrical shorts or formation of preferred current channels around the ETL/perovskite interface and, in turn, benefits the device performance.

X-ray photoelectron spectroscopy measurements were carried out on the SnO₂ QD ETL specimen to examine the chemical states of the constituent elements. Fig. 1c shows that the Sn 3d core-level spectrum exhibits the double split centered at 485.1 eV and 493.5 eV representing Sn 3d_{3/2} and Sn 3d_{5/2}, respectively. These two broad peaks and the spin-orbiting coupling energy between these two levels confirm that Sn is in 4⁺ oxidation state in SnO₂. Fig. 1d displays the high-resolution scan of the symmetrical O 1s peak at 529 eV with lower and higher binding energies from the lattice oxygen atoms in Sn–O–Sn coordinated environment and the hydroxide species (Sn–OH), respectively. The coordinated Sn–O–Sn plays as the electron conductance pathways while the hydroxide species (Sn–OH) serve as shallow trap sites [67,68].

ITO, SnO₂ QD film, and perovskite film were subjected to UV–Vis spectroscopic studies to determine their optical properties, as

shown in Fig. 2a. The optical direct bandgap (E_g) was determined by using Tauc relation to plot $(\alpha h\nu)^{1/r}$ versus energy of the photons, where r represents the nature of transition of the charge carriers and $r = 1/2$ for direct bandgap materials. From the extrapolation of the Tauc plot as shown in Fig. 2b, SnO₂ QD was determined to have a wide bandgap of ~3.72 eV which is similar to what has been previously reported [69]. This wide bandgap could be due to the imperfections in the crystal lattice, such as oxygen deficiency [70,71]. The ITO was observed to have a bandgap of 3.82 eV while perovskite layer had a bandgap of 1.53 eV. The wide bandgap of ITO and SnO₂ suggests that these materials do not interact with the photons in the visible solar spectrum, while the perovskite material interacts with the photons in the visible solar spectrum due to its narrow bandgap. The optical transmittance characteristics and the calculated optical bandgap values suggest that the perovskite film acts as an absorber while SnO₂ QDs and ITO block the UV spectrum.

Fig. 2c shows the effect of QD SnO₂ film thickness on the electrical conductivity, by varying the spin-coating speed for the deposition of SnO₂ QDs from 3000 r.p.m. to 5000 r.p.m. When the spin-coating speed was increased from 3000 r.p.m. to 5000 r.p.m., the sheet resistance of the QD SnO₂ film decreased from 15.8 to 14.2 Ω/sq. Here, the dashed line indicates that the ITO substrate was observed to have a sheet resistance of 13.3 Ω/sq. An ideal scenario would be to have a dense film with the least resistivity. Although the film deposited at 5000 r.p.m. had the least sheet resistance due to it being the thinnest film of the lot, we opted for 4000 r.p.m. as the film would be denser and hence less chances for pinholes being present in the film. Film deposited at 3000 r.p.m. would be even more dense, but due to its high resistivity it outweighs the benefits of the denser films. We also measured the resistivity of the carbon electrode on a glass substrate and the obtained results are

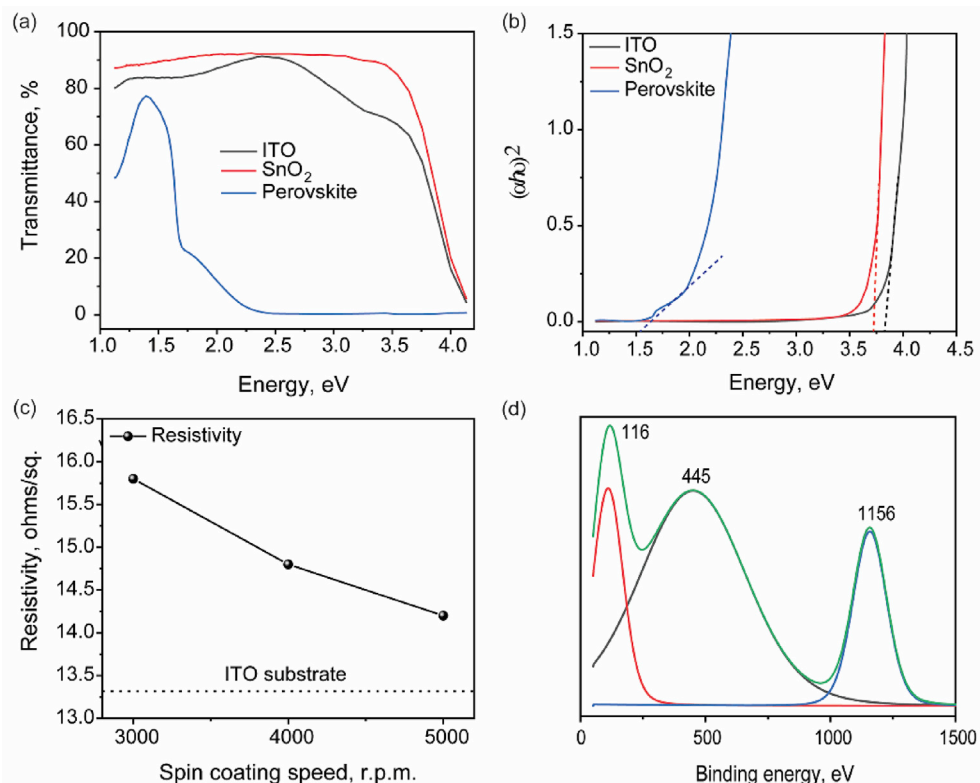


Fig. 2. (a) Transmittance spectra and (b) Tauc plot of ITO, SnO₂, and perovskite layers; (c) Comparison of the sheet resistance of ETL for different spin-coating speeds and for a bare ITO; (d) Raman spectra of triple cation perovskite. ETL, electron transport layer.

displayed in Fig. S2 in supporting information. The carbon paste was annealed at 100 °C for durations of 10, 20, and 30 min, and the sheet resistance was found to decrease from 14.6 to 13.1 Ω/sq due to evaporation of the non-conducting binder in the paste. The longer the carbon film was annealed, more binder was evaporated and hence lower the sheet resistance.

Raman spectroscopy was performed on the absorber film to detect structural and compositional variations on microscopic scale. Considering the relative instability of the absorber film, a fast decomposition of the perovskite under excessive laser light excitation was expected. Fig. 2d shows Raman spectra of triple cation perovskite film after background subtraction obtained under excitation at 532 nm. The spectra can be characterized by two structures: the broadest one from 80 to 830 cm⁻¹ and the narrower one from 880 to 1230 cm⁻¹. The fitting of the experimental data shows a much higher full width at half maximum (FWHM) of the peaks at higher wavenumber region (250–960 cm⁻¹), in agreement with their more molecular origin [72]. A low FWHM is expected for highly ordered Pb–I cage structure, which can attribute to the peaks at 116 and 1156 cm⁻¹. On the contrary, organic molecules such as methylammonium (MA) and formamidinium (FA) have several additional degrees of torsional and rotational freedom and hence can be regarded as a disordered arrangement of separated molecules [73,74].

Fig. 3a and b show an illustration of the device structure and energy level diagram of the PSC, respectively. The PSC with a simple structure of ITO/SnO₂ QDs/perovskite/carbon was designed and fabricated using spin-coating technique. The excitons generated in the perovskite leads to the injection of electrons into the conduction band of SnO₂ QDs, while the holes are injected into the carbon. The photogenerated electrons in the perovskite diffuse through to reach the SnO₂ QDs and ITO while the photoexcited holes were transferred into the carbon electrode (Fig. 4b). The surface morphology of the as-grown perovskite thin film of the device is shown in Fig. 3c. The pinhole-free perovskite films were observed to be dense and continuous with an average grain size of 300 nm. The AFM topography and the perovskite grains appear to be smooth with RMS~20 nm (refer the supporting information, Fig. S2). The grain size is relatively small compared with the reported micrometer level grain size, the potential reason is that the QD SnO₂ ETL provides additional nuclei site and suppress the grain growth during perovskite deposition and thermal annealing [75]. Moreover, when grain sizes are in the micrometer range, there is a possibility for large intercrystal cracks due to the mechanical stress from the fast crystal growth during the annealing of the film, which would lead to more defects and quantum traps. It has been previously stated that an antisolvent can reduce the solubility of the solvent in the solution without completely inhibiting it; it plays a key role in accelerating homogeneous nucleation due to

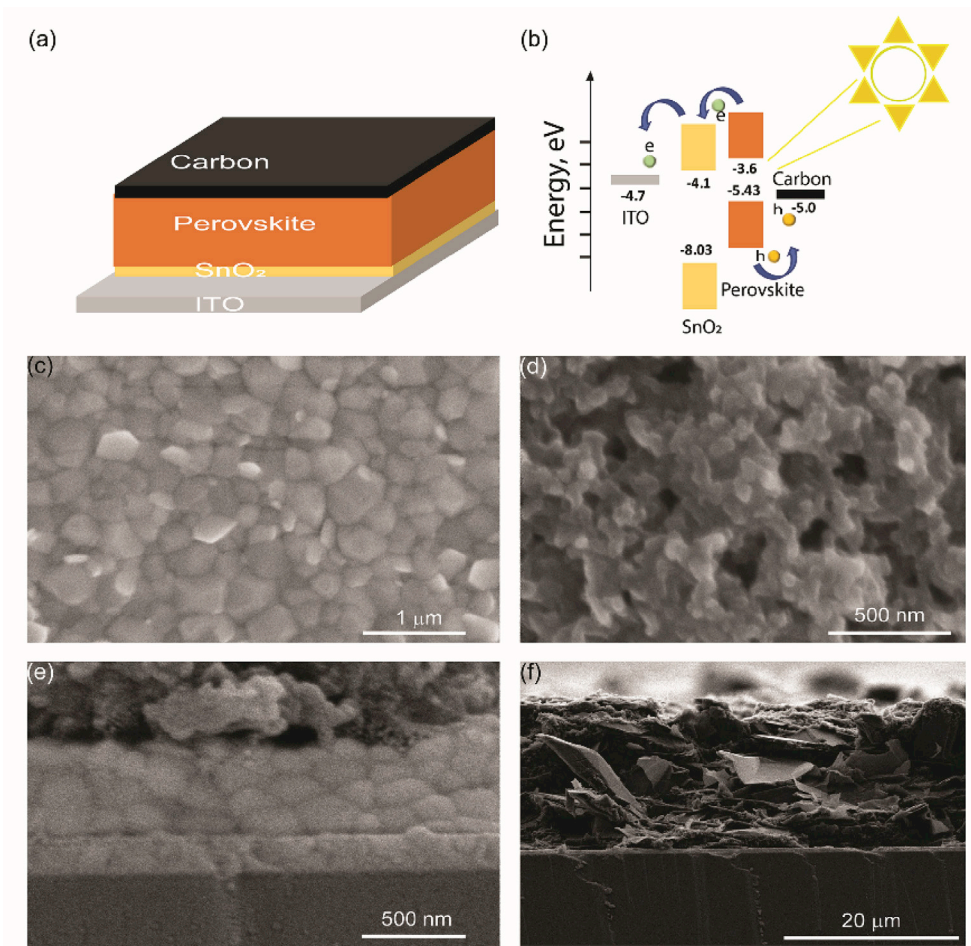


Fig. 3. (a) Schematic of the carbon-based perovskite device structure and (b) energy level diagram of individual layers used in the device without HTL; (c) Top-view SEM image of the perovskite film; (d) Top-view SEM image of the carbon electrode; (e) Cross-sectional SEM image of the perovskite solar cell device; (f) Cross-sectional SEM image of the carbon electrode. HTL, hole transport layer.

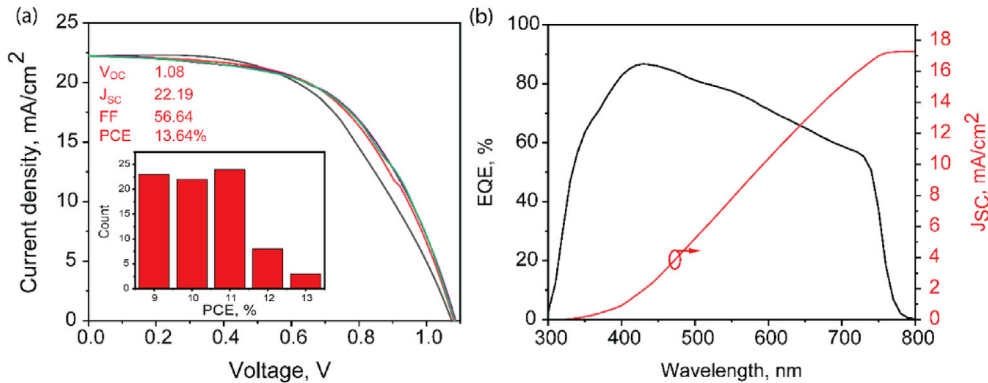


Fig. 4. (a) J-V characteristics of the PSC and the inset depicts a histogram of the PCE distribution for 80 planar PSCs; (b) EQE spectra and integrated current density of the PSC as a function of wavelength. EQE, external quantum efficiency; PSC, perovskite solar cell; PCE, power conversion efficiency.

supersaturation [56,76–78]. The antisolvent should be optimized according to the substrate area and the volume of perovskite precursor as it optimizes the film morphology and crystallization, and it can also generate the largest grain sizes and flat surface which would then benefit the subsequent layers [76]. The cross-sectional image of the PSC was shown in the Fig. 3e, where the layered (e.g. ~3 layer) nanoscale perovskite grain (~100 nm) can be observed along the film thickness, suggesting that the perovskite shows nanocrystalline grain size. This nanocrystalline perovskite grown on QD SnO₂ ETLs is different from that of the columnar perovskite grains deposited on the TiO₂ ETL or SnO₂ nanocrystalline ETLs. This nanocrystalline perovskite grain size can also originate from the fine nuclei of perovskite formed on the QD SnO₂ ETL.

Fig. 3d and f show the surface morphology and the cross-sectional view of the carbon electrode, respectively. The thickness of the carbon electrode is about 15 μm, which is much thicker than that of the perovskite layer. In addition, the carbon electrode has a lot of pores in it due to the evaporation of the binder when the carbon electrode is annealed. As illustrated in the cross-sectional SEM images, the device architecture is glass/ITO/SnO₂/perovskite/carbon. From the cross-sectional image of the device, the grains of perovskite tend to stack on top of each other forming highly oriented grains perpendicular to the substrate. No voids were observed in the cross-sectional view of the absorber layer which could have acted as a recombination center to impede the charge carrier collection during the operation of the device.

We identified SnO₂ 0.15 M QD as the best suited ETL after several screening of different concentrations of SnO₂ QD and SnO₂ colloid. Table 1 and Fig. S3a show the comparison of electrical characteristics of PSCs with SnO₂ colloid (3% volume fraction in DIW), 0.15 M and 0.1 M SnO₂ QDs as ETLs. Although there are reports that attribute PCE of ~20% for PSCs using SnO₂ colloid, our PSC with SnO₂ colloid had the worst performance because of the poor charge transfer capability [79]. Unlike the SnO₂ QDs, the ETL synthesized with colloid SnO₂ had high trap density present in the material

which impeded the diffusion of the charge carriers toward the ITO. Because of the inefficient collection of electrons, the J_{SC} was much lower than that of the cells with QD ETLs and it also contributed toward an unimpressive FF. These issues were addressed by the scientific community by using a very thin phenyl-C61-butyric acid methyl ester (PCBM) layer on the SnO₂ layer to enhance electron transport and suppress the recombination [80]. EDTA-complexed SnO₂ was synthesized by Yang et al. [28], Zuo et al [29], and Yang et al [81] to boost the electron mobility, and multiple other groups used self-assembled monolayers to passivate the trap states present at the interface. Although the cell with SnO₂ colloid delivers a comparable V_{OC} as that with the SnO₂ QD ETL, the poor J_{SC} and FF resulted in reduced PCE. Among the cells with SnO₂ QD ETLs, the cell that was fabricated with 0.15 M precursor showed an improved performance due to the dense ETL because of the increased concentration of the precursor. The concentration increase contributed to the pinhole free and well-connected ETLs as shown in Fig. 3c which contributed to improved collection of the charge carriers. But upon further increase of the precursor concentration to 0.17 M, the electrical performance of the device was found to take a hit. We believe this is because of the increased thickness of ETLs which would then act as a blocking layer for the electrons from reaching ITO and hence hinders the efficient collection of charge carriers.

Table 2 and Fig. S3b show the impact of change in spin-coating speed of SnO₂ 0.15 M ETLs on the device performance. The device with SnO₂ 0.15 M ETLs deposited at 4000 r.p.m. gave the best performance. When the speed was reduced to 3000 r.p.m., the PCE reduced because the SnO₂ ETL became thicker and hence blocked the charge diffusion toward ITO as was the case when the precursor concentration increased. When the spin-coating speed was increased to 5000 r.p.m., the ETL became thinner and hence resulted in an ineffective hole blocking. This resulted in increased recombination of charge carriers and hence the J_{SC} reduced which adversely affected the FF and PCE of the device. These tests gave us a conclusive evidence that 4000 r.p.m. is the best speed for the deposition of ETLs.

The champion device based on SnO₂ QD ETLs delivers a PCE of 13.64%, with a V_{OC} of 1.08 V, J_{SC} of 22.19 mA/cm², and FF of 56.64% measured under reverse scan conditions. This impressive performance was reproducible as shown in Fig. 4a which compares the J-V characteristics of multiple cells fabricated under the same conditions. These measurements were carried out in ambient air under AM 1.5 illumination at the light intensity 100 mW/cm². V_{OC} of our champion device is better than what is already reported for the best performing carbon-based HTL-free devices, while the J_{SC} matches with the reported values [82,83]. The FF is related to the shunt

Table 1

Comparison of J-V parameters of PSCs measured under AM1.5G illumination at 100 mWcm⁻² with different SnO₂ ETL.

SnO ₂ details	V _{OC} (V)	J _{SC} (mAcm ⁻²)	FF (%)	R _{OC}	R _{SC}	PCE (%)
0.15 M QD	1.08	22.19	56.64	134.93	11845.48	13.64
0.1 M QD	1.05	20.17	52.95	162.41	6465.25	11.22
0.17 M QD	1.09	14.68	53.72	238.78	19473.06	8.59
3% colloid	1.04	18.35	44.27	201.55	3965.53	8.42

PCE, power conversion efficiency; FF, fill factor; QD, quantum dot; PSC, perovskite solar cell; ETL, electron transport layer.

Table 2

Comparison of key J-V parameters of PSCs measured under AM1.5G illumination at 100 mW cm⁻² with SnO₂ 0.15 M QD ETL spin-coated at various speeds.

SnO ₂ details	Spin-coating speed (r.p.m.)	V _{OC} (V)	J _{SC} (mAc m ⁻²)	FF (%)	R _{OC}	R _{SC}	PCE (%)
0.15 M QD	3000	1.05	20.16	52.95	162.41	6465.26	11.22
0.15 M QD	4000	1.08	22.19	56.64	134.93	11845.48	13.64
0.15 M QD	5000	1.1	19.02	49.55	198.01	4903.34	10.35

PCE, power conversion efficiency; QD, quantum dot; ETL, electron transport layer; PSC, perovskite solar cell.

resistance, R_{sh}, and the series resistance, R_s, by the factor R_{sh}/R_s. The comparatively poor FF was due to the inefficient contact between the perovskite layer and the carbon electrode which results in poor charge transfer between these layers and hence an increased R_s. Mishra et al. [84] did a detailed study on the effect of annealing temperature on the morphology of screen-printed carbon [85]. It was observed that sintering temperature above 300 °C ensured better contact between particles, which would enable faster and efficient transport of charge carriers and better conductivity. A highly mesoporous structure with pore filling capability was created this way. Moreover, when the carbon paste is annealed at temperature below 300 °C, highly resistive electrodes with poor perovskite infiltration was obtained. But, annealing the carbon electrode at these high temperatures would beat one of the major goals of our work, which is to synthesis 'low-temperature processed materials' to make flexible PSCs a possibility. The absence of an HTL too played a role in the inefficient transport of charge carriers which resulted in a reduced FF. The inset in Fig. 4a is a histogram of PCE values for the 80 cells demonstrating that the devices exhibit an average PCE of 10.32%.

Fig. 4b shows the EQE with 17.3 mA/cm² as the integrated value of J_{SC}. This value is lower than what has been derived from J-V curves due to the absence of light-soaking during EQE measurements. It generally takes a few seconds for light soaking to stabilize the photocurrent of the cell [86–89]. There is a decline in the quantum efficiency values from ~410 nm due to the inefficient interface between the absorber layer and the back contact. This suggests that the holes being generated in the perovskite layer are not efficiently transferred to the carbon electrode. This could be due to the inefficient contact between the carbon and perovskite layers due to the pores present in the carbon, and hence the carbon layer is not able to uniformly touch the entire surface of the perovskite layer. Further interfacial engineering by inserting low-cost HTLs may address this issue.

4. Conclusions

In conclusion, we successfully fabricated highly efficient and reproducible PSCs by replacing TiO₂ with low-temperature processed SnO₂ QD ETLs and carbon electrodes. Using the optimized parameters for all the functional layers in the device, we fabricated a planar PSC with a champion PCE of 13.64%. The cells fabricated with SnO₂ QD precursors of different concentrations showed similar impressive performance while SnO₂ colloid could not match the same. The experimental results reveal that the excellent performance is ascribed to the outstanding optoelectronic properties of the SnO₂ QD ETL and the perovskite, such as good conductivity and narrow bandgap, respectively. Owing to the low-temperature processability of SnO₂ QD ETLs, this work promises a pathway toward high-quality cheap and flexible PSCs for commercial applications.

Declaration of Competing Interest

The authors declare no conflict of interest.

CRediT authorship contribution statement

S.N. Vijayaraghavan: Conceptualization, Methodology, Writing - original draft. **J. Wall:** Conceptualization, Methodology. **L. Li:** Writing - review & editing, Supervision. **G. Xing:** Writing - review & editing, Supervision. **Q. Zhang:** Writing - review & editing, Supervision. **F. Yan:** Conceptualization, Writing - review & editing, Project administration, Supervision, Funding acquisition.

Acknowledgements

S.N.V, J. W, L.P. G, and F. Y acknowledge the support from the Alabama Water Institute inThe University of Alabama and National Science Foundation under Grant No. 1844210.

Appendix A. Supplementary data

Supplementary data to this article can be found online at <https://doi.org/10.1016/j.mtphys.2020.100204>.

References

- [1] L. Xu, X.F. Chen, J.J. Jin, W. Liu, B. Dong, X. Bai, H.W. Song, P. Reiss, Inverted perovskite solar cells employing doped NiO hole transport layers: a review, *Nanomater. Energy* 63 (2019): 103860.
- [2] X.Z. Wu, High-efficiency polycrystalline CdTe thin-film solar cells, *Sol. Energy* 77 (2004) 803–814.
- [3] Y.L. Lin, *Organic Photovoltaics Using Multiple Exciton Effects*, Princeton University, 2019.
- [4] J.W. Gong, J. Liang, K. Sumathy, Review on dye-sensitized solar cells (DSSCs): fundamental concepts and novel materials, *Renew. Sustain. Energy Rev.* 16 (2012) 5848–5860.
- [5] T. Sogabe, Q. Shen, K. Yamaguchi, Recent progress on quantum dot solar cells: a review, *J. Photon. Energy* 6 (2016): 040901.
- [6] H. Choi, C. Nahm, J. Kim, C. Kim, S. Kang, T. Hwang, B. Park, Review paper: toward highly efficient quantum-dot- and dye-sensitized solar cells, *Curr. Appl. Phys.* 13 (2013) S2–S13.
- [7] S.N. Vijayaraghavan, A. Ashok, G. Gopakumar, H. Menon, S.V. Nair, M. Shanmugam, All spray pyrolysis-coated CdTe–TiO₂ heterogeneous films for photo-electrochemical solar cells, *Mater. Renew. Sustain. Energy* 7 (2018) 12.
- [8] L. Guo, B. Zhang, S. Li, A. Montgomery, L. Li, G. Xing, Q. Zhang, X. Qian, F. Yan, Interfacial engineering of oxygenated chemical bath-deposited CdS window layer for highly efficient Sb2Se3 thin-film solar cells, *Mater. Today Phys.* 10 (2019) 100125.
- [9] A. Polman, M. Knight, E.C. Garnett, B. Ehrler, W.C. Sinke, Photovoltaic materials: present efficiencies and future challenges, *Science* 352 (2016) 4424.
- [10] A. Kojima, K. Teshima, Y. Shirai, T. Miyasaka, Organometal halide perovskites as visible-light sensitizers for photovoltaic cells, *J. Am. Chem. Soc.* 131 (2009) 6050.
- [11] J. Huang, Y. Yuan, Y. Shao, Y. Yan, Understanding the physical properties of hybrid perovskites for photovoltaic applications, *Nat. Rev. Mater.* 2 (2017) 1–8.
- [12] F.Y. Wang, Y.H. Zhang, M.F. Yang, L. Fan, L.L. Yang, Y.R. Sui, J.H. Yang, X.D. Zhang, Toward ultra-thin and omnidirectional perovskite solar cells: concurrent improvement in conversion efficiency by employing light-trapping and recrystallizing treatment, *Nanomater. Energy* 60 (2019) 198–204.
- [13] L. Yang, Y. Gao, Y. Wu, X. Xue, F. Wang, Y. Sui, Y. Sun, M. Wei, X. Liu, H. Liu, Novel insight into the role of chlorobenzene antisolvent engineering for highly efficient perovskite solar cells: gradient diluted chlorine doping, *ACS Appl. Mater. Interfaces* 11 (2019) 792–801.
- [14] H. Tsai, W. Nie, J.C. Blancon, C.C. Stoumpos, R. Asadpour, B. Harutyunyan, A.J. Neukirch, R. Verduzco, J.J. Crochet, S. Tretiak, L. Pedesseau, J. Even, M.A. Alam, G. Gupta, J. Lou, P.M. Ajayan, M.J. Bedzyk, M.G. Kanatzidis, High-

- efficiency two-dimensional Ruddlesden-Popper perovskite solar cells, *Nature* 536 (2016) 312.
- [15] D.Q. Bi, C.Y. Yi, J.S. Luo, J.D. Decoppet, F. Zhang, S.M. Zakeeruddin, X. Li, A. Hagfeldt, M. Gratzel, Polymer-templated nucleation and crystal growth of perovskite films for solar cells with efficiency greater than 21%, *Nat. Energy* 1 (2016) 1–5.
- [16] W.S. Yang, B.W. Park, E.H. Jung, N.J. Jeon, Y.C. Kim, D.U. Lee, S.S. Shin, J. Seo, E.K. Kim, J.H. Noh, S.I. Seok, Iodide management in formamidinium-lead-halide-based perovskite layers for efficient solar cells, *Science* 356 (2017) 1376–1379.
- [17] F. Wang, M. Yang, Y. Zhang, L. Yang, L. Fan, S. Lv, X. Liu, D. Han, J. Yang, Activating old materials with new architecture: boosting performance of perovskite solar cells with H₂O-assisted hierarchical electron transporting layers, *Adv. Sci.* 6 (2019) 1801170.
- [18] J.H. Heo, S.H. Im, J.H. Noh, T.N. Mandal, C.S. Lim, J.A. Chang, Y.H. Lee, H.J. Kim, A. Sarkar, M.K. Nazeeruddin, M. Gratzel, S.I. Seok, Efficient inorganic-organic hybrid heterojunction solar cells containing perovskite compound and polymeric hole conductors, *Nat. Photon.* 7 (2013) 487–492.
- [19] H. Chen, X. Pan, W. Liu, M. Cai, D. Kou, Z. Huo, X. Fang, S. Dai, Efficient panchromatic inorganic-organic heterojunction solar cells with consecutive charge transport tunnels in hole transport material, *Chem. Commun.* 49 (2013) 7277–7279.
- [20] A.Y. Mei, X. Li, L.F. Liu, Z.L. Ku, T.F. Liu, Y.G. Rong, M. Xu, M. Hu, J.Z. Chen, Y. Yang, M. Gratzel, H.W. Han, A hole-conductor-free, fully printable mesoscopic perovskite solar cell with high stability, *Science* 345 (2014) 295–298.
- [21] J.M. Ball, M.M. Lee, A. Hey, H.J. Snaith, Low-temperature processed meso-superstructured to thin-film perovskite solar cells, *Energy Environ. Sci.* 6 (2013) 1739–1743.
- [22] T. Leijtens, G.E. Eperon, S. Pathak, A. Abate, M.M. Lee, H.J. Snaith, Overcoming ultraviolet light instability of sensitized TiO₂) with meso-superstructured organometal tri-halide perovskite solar cells, *Nat. Commun.* 4 (2013) 2885.
- [23] B. Roose, J.P.C. Baena, K.C. Godel, M. Graetzel, A. Hagfeldt, U. Steiner, A. Abate, Mesoporous SnO₂ electron selective contact enables UV-stable perovskite solar cells, *Nanomater. Energy* 30 (2016) 517–522.
- [24] K. Wojciechowski, T. Leijtens, S. Siprova, C. Schlueter, M.T. Horantner, J.T. Wang, C.Z. Li, A.K. Jen, T.L. Lee, H.J. Snaith, C60 as an efficient n-type compact layer in perovskite solar cells, *J. Phys. Chem. Lett.* 6 (2015) 2399–2405.
- [25] Y.B. Gao, L.L. Yang, F.Y. Wang, Y.R. Sui, Y.F. Sun, M.B. Wei, J. Cao, H.L. Liu, Anti-solvent surface engineering via diethyl ether to enhance the photovoltaic conversion efficiency of perovskite solar cells to 18.76%, *Superlattice. Microst.* 113 (2018) 761–768.
- [26] P. Tiwana, P. Docampo, M.B. Johnston, H.J. Snaith, L.M. Herz, Electron mobility and injection dynamics in mesoporous ZnO, SnO₂, and TiO₂ films used in dye-sensitized solar cells, *ACS Nano* 5 (2011) 5158.
- [27] E.H. Anaraki, A. Kermanpur, L. Steier, K. Domanski, T. Matsui, W. Tress, M. Saliba, A. Abate, M. Gratzel, A. Hagfeldt, J.P. Correa-Baena, Highly efficient and stable planar perovskite solar cells by solution-processed tin oxide, *Energy Environ. Sci.* 9 (2016) 3128–3134.
- [28] G. Yang, C.L. Wang, H.W. Lei, X.L. Zheng, P.L. Qin, L.B. Xiong, X.Z. Zhao, Y.F. Yan, G.J. Fang, Interface engineering in planar perovskite solar cells: energy level alignment, perovskite morphology control and high performance achievement, *J. Mater. Chem. 5* (2017) 1658–1666.
- [29] L. Zuo, Q. Chen, N. De Marco, Y.T. Hsieh, H. Chen, P. Sun, S.Y. Chang, H. Zhao, S. Dong, Y. Yang, Tailoring the interfacial chemical interaction for high-efficiency perovskite solar cells, *Nano Lett.* 17 (2017) 269–275.
- [30] J.P.C. Baena, L. Steier, W. Tress, M. Saliba, S. Neutzner, T. Matsui, F. Giordano, T.J. Jacobsson, A.R.S. Kandala, S.M. Zakeeruddin, M. Graetzel, A. Petrozza, A. Abate, M.K. Nazeeruddin, M. Gratzel, A. Hagfeldt, Highly efficient planar perovskite solar cells through band alignment engineering, *Energy Environ. Sci.* 8 (2015) 2928–2934.
- [31] H.J. Snaith, C. Ducati, SnO₂-based dye-sensitized hybrid solar cells exhibiting near unity absorbed photon-to-electron conversion efficiency, *Nano Lett.* 10 (2010) 1259.
- [32] W.J. Ke, D.W. Zhao, A.J. Cimaroli, C.R. Grice, P.L. Qin, Q. Liu, L.B. Xiong, Y.F. Yan, G.J. Fang, Effects of annealing temperature of tin oxide electron selective layers on the performance of perovskite solar cells, *J. Mater. Chem. 3* (2015) 24163–24168.
- [33] G.L. Shang, J.H. Wu, M.L. Huang, J.M. Lin, Z. Lan, Y.F. Huang, L.Q. Fan, Facile synthesis of mesoporous tin oxide spheres and their applications in dye-sensitized solar cells, *J. Phys. Chem. C* 116 (2012) 20140–20145.
- [34] G.L. Shang, J.H. Wu, S. Tang, M.L. Huang, Z. Lan, Y. Li, J.C. Zhao, X.P. Zhang, Preparation of hierarchical tin oxide microspheres and their application in dye-sensitized solar cells, *J. Mater. Chem. 22* (2012) 25335–25339.
- [35] Y.F. Wang, X.F. Li, D.J. Li, Y.W. Sun, X.X. Zhang, Controllable synthesis of hierarchical SnO₂ microspheres for dye-sensitized solar cells, *J. Power Sources* 280 (2015) 476–482.
- [36] G. Yang, C. Chen, F. Yao, Z. Chen, Q. Zhang, X. Zheng, J. Ma, H. Lei, P. Qin, L. Xiong, W. Ke, G. Li, Y. Yan, G. Fang, Effective carrier-concentration tuning of SnO₂ quantum dot electron-selective layers for high-performance planar perovskite solar cells, *Adv. Mater.* 30 (2018) 1706023.
- [37] V.T. Chebrolu, H.J. Kim, Recent progress in quantum dot sensitized solar cells: an inclusive review of photoanode, sensitizer, electrolyte, and the counter electrode, *J. Mater. Chem. C* 7 (2019) 4911–4933.
- [38] S. Ameen, M.A. Rub, S.A. Kosa, K.A. Alamry, M.S. Akhtar, H.S. Shin, H.K. Seo, A.M. Asiri, M.K. Nazeeruddin, Perovskite solar cells: influence of hole transporting materials on power conversion efficiency, *ChemSusChem* 9 (2016) 10–27.
- [39] C. Bi, Q. Wang, Y. Shao, Y. Yuan, Z. Xiao, J. Huang, Non-wetting surface-driven high-aspect-ratio crystalline grain growth for efficient hybrid perovskite solar cells, *Nat. Commun.* 6 (2015) 7747.
- [40] W.Q. Wu, D.H. Chen, F. Li, A.R. Pascoe, Y.B. Cheng, R.A. Caruso, Integrated planar and bulk dual heterojunctions capable of efficient electron and hole extraction for perovskite solar cells with > 17% efficiency, *Nanomater. Energy* 32 (2017) 187–194.
- [41] W.Q. Wu, Q. Wang, Y. Fang, Y. Shao, S. Tang, Y. Deng, H. Lu, Y. Liu, T. Li, Z. Yang, A. Gruber, J. Huang, Molecular doping enabled scalable blading of efficient hole-transport-layer-free perovskite solar cells, *Nat. Commun.* 9 (2018) 1625.
- [42] S. Ye, W. Sun, Y. Li, W. Yan, H. Peng, Z. Bian, Z. Liu, C. Huang, CuSCN-based inverted planar perovskite solar cell with an average PCE of 15.6%, *Nano Lett.* 15 (2015) 3723–3727.
- [43] S. Akin, Y.H. Liu, M.I. Dar, S.M. Zakeeruddin, M. Gratzel, S. Turan, S. Sonmezoglu, Hydrothermally processed CuCrO₂ nanoparticles as an inorganic hole transporting material for low-cost perovskite solar cells with superior stability, *J. Mater. Chem. 6* (2018) 20327–20337.
- [44] J.V. Milic, D.J. Kubicki, L. Emsley, M. Gratzel, Multifunctional molecular modulation for efficient and stable hybrid perovskite solar cells, *Chimia* 73 (2019) 317–323.
- [45] Z.N. Song, C.L. McElvany, A.B. Phillips, I. Celik, P.W. Krantz, S.C. Watthage, G.K. Liyanage, D. Apul, M.J. Heben, A technoeconomic analysis of perovskite solar module manufacturing with low-cost materials and techniques, *Energy Environ. Sci.* 10 (2017) 1297–1305.
- [46] W. Abu Laban, L. Etgar, Depleted hole conductor-free lead halide heterojunction solar cells, *Energy Environ. Sci.* 6 (2013) 3249–3253.
- [47] S. Aharon, S. Gamliel, B. El Cohen, L. Etgar, Depletion region effect of highly efficient hole conductor free CH₃NH₃PbI₃ perovskite solar cells, *Phys. Chem. Chem. Phys.* 16 (2014) 10512–10518.
- [48] L. Etgar, Semiconductor nanocrystals as light harvesters in solar cells, *Materials* 6 (2013) 445–459.
- [49] S.D. Stranks, G.E. Eperon, G. Grancini, C. Menelaou, M.J. Alcocer, T. Leijtens, L.M. Herz, A. Petrozza, H.J. Snaith, Electron-hole diffusion lengths exceeding 1 micrometer in an organometal trihalide perovskite absorber, *Science* 342 (2013) 341.
- [50] G. Xing, N. Mathews, S. Sun, S.S. Lim, Y.M. Lam, M. Gratzel, S. Mhaisalkar, T.C. Sum, Long-range balanced electron- and hole-transport lengths in organic-inorganic CH₃NH₃PbI₃, *Science* 342 (2013) 344.
- [51] H.N. Chen, Z.H. Wei, H.X. He, X.L. Zheng, K.S. Wong, S.H. Yang, Solvent engineering boosts the efficiency of paintable carbon-based perovskite solar cells to beyond 14%, *Adv. Energy Mater.* 6 (2016) 1502087.
- [52] Z. Ku, Y. Rong, M. Xu, T. Liu, H. Han, Full printable processed mesoscopic CH(3) NH(3)PbI(3)/TiO(2) heterojunction solar cells with carbon counter electrode, *Sci. Rep.-Uk* 3 (2013) 3132.
- [53] X. Li, M. Tschumi, H.W. Han, S.S. Babkair, R.A. Alzubaydi, A.A. Ansari, S.S. Habib, M.K. Nazeeruddin, S.M. Zakeeruddin, M. Gratzel, Outdoor performance and stability under elevated temperatures and long-term light soaking of triple-layer mesoporous perovskite photovoltaics, *Energy Technol.-Ger* 3 (2015) 551–555.
- [54] Z.H. Wei, K.Y. Yan, H.N. Chen, Y. Yi, T. Zhang, X. Long, J.K. Li, L.X. Zhang, J.N. Wang, S.H. Yang, Cost-efficient clamping solar cells using candle soot for hole extraction from ambipolar perovskites, *Energy Environ. Sci.* 7 (2014) 3326–3333.
- [55] Z.H. Wei, X.L. Zheng, H.N. Chen, X. Long, Z.L. Wang, S.H. Yang, A multifunctional C plus epoxy/Ag-paint cathode enables efficient and stable operation of perovskite solar cells in watery environments, *J. Mater. Chem. 3* (2015) 16430–16434.
- [56] Y.Y. Zhou, M.J. Yang, A.L. Vasiliev, H.F. Garces, Y.X. Zhao, D. Wang, S.P. Pang, K. Zhu, N.P. Padture, Growth control of compact CH₃NH₃PbI₃ thin films via enhanced solid-state precursor reaction for efficient planar perovskite solar cells, *J. Mater. Chem. 3* (2015) 9249–9256.
- [57] K. Aitola, K. Sveinbjornsson, J.P. Correa-Baena, A. Kaskela, A. Abate, Y. Tian, E.M.J. Johansson, M. Gratzel, E.I. Kauppinen, A. Hagfeldt, G. Boschloo, Carbon nanotube-based hybrid hole-transporting material and selective contact for high efficiency perovskite solar cells, *Energy Environ. Sci.* 9 (2016) 461–466.
- [58] S. Gholipour, J.P. Correa-Baena, K. Domanski, T. Matsui, L. Steier, F. Giordano, F. Tajabadi, W. Tress, M. Saliba, A. Abate, A.M. Ali, N. Taghavinia, M. Gratzel, A. Hagfeldt, Highly efficient and stable perovskite solar cells based on a low-cost carbon cloth, *Adv. Energy Mater.* 6 (2016) 1601116.
- [59] C.M. Tsai, G.W. Wu, S. Narra, H.M. Chang, N. Mohanta, H.P. Wu, C.L. Wang, E.W.G. Diau, Control of preferred orientation with slow crystallization for carbon-based mesoscopic perovskite solar cells attaining efficiency 15%, *J. Mater. Chem. 5* (2017) 739–747.
- [60] H.Y. Wei, J.Y. Xiao, Y.Y. Yang, S.T. Lv, J.J. Shi, X. Xu, J. Dong, Y.H. Luo, D.M. Li, Q.B. Meng, Free-standing flexible carbon electrode for highly efficient hole-conductor-free perovskite solar cells, *Carbon* 93 (2015) 861–868.
- [61] Z.H. Wei, H.N. Chen, K.Y. Yan, X.L. Zheng, S.H. Yang, Hysteresis-free multi-walled carbon nanotube-based perovskite solar cells with a high fill factor, *J. Mater. Chem. 3* (2015) 24226–24231.

- [62] Y. Hu, Z. Zhang, A. Mei, Y. Jiang, X. Hou, Q. Wang, K. Du, Y. Rong, Y. Zhou, G. Xu, H. Han, Improved performance of printable perovskite solar cells with bifunctional conjugated organic molecule, *Adv. Mater.* 30 (2018): 1705786.
- [63] Z. Liu, B. Sun, X. Liu, J. Han, H. Ye, Y. Tu, C. Chen, T. Shi, Z. Tang, G. Liao, 15% efficient carbon based planar-heterojunction perovskite solar cells using a TiO₂/SnO₂ bilayer as the electron transport layer, *J. Mater. Chem. C* 6 (2018) 7409–7419.
- [64] J. Jiang, Z. Jin, F. Gao, J. Sun, Q. Wang, S.F. Liu, CsPbCl₃-Driven low-trap-density perovskite grain growth for >20% solar cell efficiency, *Adv. Sci.* 5 (2018): 1800474.
- [65] Q. Jiang, Z. Chu, P. Wang, X. Yang, H. Liu, Y. Wang, Z. Yin, J. Wu, X. Zhang, J. You, Planar-structure perovskite solar cells with efficiency beyond 21%, *Adv. Mater.* 29 (2017): 1703852.
- [66] B.W. Park, N. Kedem, M. Kulbak, D.Y. Lee, W.S. Yang, N.J. Jeon, J. Seo, G. Kim, K.J. Kim, T.J. Shin, G. Hodes, D. Cahen, S.I. Seok, Understanding how excess lead iodide precursor improves halide perovskite solar cell performance, *Nat. Commun.* 9 (2018) 3301.
- [67] K.K. Banger, Y. Yamashita, K. Mori, R.L. Peterson, T. Leedham, J. Rickard, H. Sirringhaus, Low-temperature, high-performance solution-processed metal oxide thin-film transistors formed by a 'sol-gel on chip' process, *Nat. Mater.* 10 (2011) 45–50.
- [68] L.B. Qiu, Z.H. Liu, L.K. Ono, Y. Jiang, D.Y. Son, Z. Hawash, S.S. He, Y.B. Qi, Scalable fabrication of stable high efficiency perovskite solar cells and modules utilizing room temperature sputtered SnO₂ electron transport layer, *Adv. Funct. Mater.* 29 (2019): 1806779.
- [69] M. Batzill, U. Diebold, The surface and materials science of tin oxide, *Prog. Surf. Sci.* 79 (2005) 47–154.
- [70] V. Kumar, V. Kumar, S. Som, J.H. Neethling, M. Lee, O.M. Ntwaeborwa, H.C. Swart, The role of surface and deep-level defects on the emission of tin oxide quantum dots, *Nanotechnology* 25 (2014): 135701.
- [71] J. Liu, W. Xue, G. Jin, Z. Zhai, J. Lv, W. Hong, Y. Chen, Preparation of tin oxide quantum dots in aqueous solution and applications in semiconductor gas sensors, *Nanomaterials-Basel* 9 (2019): 9020240.
- [72] P. Pistor, A. Ruiz, A. Cabot, V. Izquierdo-Roca, Advanced Raman spectroscopy of methylammonium lead iodide: development of a non-destructive characterisation methodology, *Sci. Rep.-Uk* 6 (2016) 35973.
- [73] E. Mosconi, A. Amat, M.K. Nazeeruddin, M. Gratzel, F. De Angelis, First-principles modeling of mixed halide organometal perovskites for photovoltaic applications, *J. Phys. Chem. C* 117 (2013) 13902–13913.
- [74] C. Quarti, G. Grancini, E. Mosconi, P. Bruno, J.M. Ball, M.M. Lee, H.J. Snaith, A. Petrozza, F.D. Angelis, The Raman spectrum of the CH₃NH₃PbI₃ hybrid perovskite: interplay of theory and experiment, *J. Phys. Chem. Lett.* 5 (2014) 279–284.
- [75] L.F. Li, P. Zhou, J. Li, Y.P. Mo, W.C. Huang, J.Y. Xiao, W. Li, Z.L. Ku, J. Zhong, Y. Peng, Y.B. Cheng, F.Z. Huang, Suppressed hysteresis and enhanced performance of triple cation perovskite solar cell with chlorine incorporation, *J. Mater. Chem. C* 6 (2018) 13157–13161.
- [76] M. Xiao, L. Zhao, M. Geng, Y. Li, B. Dong, Z. Xu, L. Wan, W. Li, S. Wang, Selection of an anti-solvent for efficient and stable cesium-containing triple cation planar perovskite solar cells, *Nanoscale* 10 (2018) 12141–12148.
- [77] F. Hao, C.C. Stoumpos, P. Guo, N. Zhou, T.J. Marks, R.P. Chang, M.G. Kanatzidis, Solvent-mediated crystallization of CH₃NH₃PbI₃ films for heterojunction depleted perovskite solar cells, *J. Am. Chem. Soc.* 137 (2015) 11445–11452.
- [78] S.S. Liu, W.C. Huang, P.Z. Liao, N. Pootrakulchote, H. Li, J.F. Lu, J.P. Li, F.H. Huang, X.X. Shai, X.J. Zhao, Y. Shen, Y.B. Cheng, M.K. Wang, 17% efficient printable mesoscopic PIN metal oxide framework perovskite solar cells using cesium-containing triple cation perovskite (vol 5, pg 22952, 2017), *J. Mater. Chem. C* 6 (2018), 4220–4220.
- [79] Y. Luan, X. Yi, P. Mao, Y. Wei, J. Zhuang, N. Chen, T. Lin, C. Li, J. Wang, High-performance planar perovskite solar cells with negligible hysteresis using 2,2,2-trifluoroethanol-incorporated SnO₂, *Iscience* 16 (2019) 433–441.
- [80] W.J. Ke, D.W. Zhao, C.X. Xiao, C.L. Wang, A.J. Cimaroli, C.R. Grice, M.J. Yang, Z. Li, C.S. Jiang, M. Al-Jassim, K. Zhu, M.G. Kanatzidis, G.J. Fang, Y.F. Yan, Cooperative tin oxide fullerene electron selective layers for high-performance planar perovskite solar cells, *J. Mater. Chem. C* 4 (2016) 14276–14283.
- [81] D. Yang, R. Yang, K. Wang, C. Wu, X. Zhu, J. Feng, X. Ren, G. Fang, S. Priya, S.F. Liu, High efficiency planar-type perovskite solar cells with negligible hysteresis using EDTA-complexed SnO₂, *Nat. Commun.* 9 (2018) 3239.
- [82] Y.L. Yang, Z.H. Liu, W.K. Ng, L.H. Zhang, H. Zhang, X.Y. Meng, Y. Bai, S. Xiao, T. Zhang, C. Hu, K.S. Wong, S.H. Yang, An ultrathin ferroelectric perovskite oxide layer for high-performance hole transport material free carbon based halide perovskite solar cells, *Adv. Funct. Mater.* 29 (2019): 1806506.
- [83] J.S. Zhou, J. Hou, X. Tao, X.Y. Meng, S.H. Yang, Solution-processed electron transport layer of n-doped fullerene for efficient and stable all carbon based perovskite solar cells, *J. Mater. Chem. C* 7 (2019) 7710–7716.
- [84] A. Mishra, Z. Ahmad, I. Zimmermann, D. Martineau, R.A. Shakoor, F. Touati, K. Riaz, S.A. Al-Muhtaseb, M.K. Nazeeruddin, Effect of annealing temperature on the performance of printable carbon electrodes for perovskite solar cells, *Org. Electron.* 65 (2019) 375–380.
- [85] L. Fagiolari, F. Bella, Carbon-based materials for stable, cheaper and large-scale processable perovskite solar cells, *Energy Environ. Sci.* 12 (2019) 3437–3472.
- [86] Y. Jiang, J. Yuan, Y. Ni, J. Yang, Y. Wang, T. Jiu, M. Yuan, J. Chen, Reduced-dimensional α -CsPbX₃ perovskites for efficient and stable photovoltaics, *Joule* 2 (2018) 1356–1368.
- [87] C.F.J. Lau, X. Deng, Q. Ma, J. Zheng, J.S. Yun, M.A. Green, S. Huang, A.W. Ho-Baillie, CsPbI₂ perovskite solar cell by spray-assisted deposition, *ACS Energy Lett.* 1 (2016) 573–577.
- [88] Q. Zhang, W. Zhu, D. Chen, Z. Zhang, Z. Lin, J. Chang, J. Zhang, C. Zhang, Y. Hao, Light processing enables efficient carbon-based, all-inorganic planar CsPbI₂solar cells with high photovoltages, *ACS Appl. Mater. Interfaces* 11 (2019) 2997–3005.
- [89] W.D. Zhu, Z.Y. Zhang, W.M. Chai, D.Z. Chen, H. Xi, J.J. Chang, J.C. Zhang, C.F. Zhang, Y. Hao, Benign pinholes in CsPbI₂ absorber film enable efficient carbon-based, all-inorganic perovskite solar cells, *ACS Appl. Energy Mater.* 2 (2019) 5254–5262.